Microchemical Journal 215 (2025) 114455

Contents lists available at ScienceDirect

Microchemical Journal

journal homepage: www.elsevier.com/locate/microc

Ultrasensitive electrochemical biosensor using Carboxylated graphitic carbon nitride-nanogold composite for SARS-CoV-2 receptor binding protein

P.R. Ramya [a,b], Shivmuni Sarup [a], Ivan Jerman [c], Raghuraj Singh Chouhan [d,*], Sonu Gandhi [a,b,**]

[a] BRIC-National Institute of Animal Biotechnology (NIAB), Hyderabad 500032, Telangana, India
[b] BRIC-Regional Centre for Biotechnology (RCB), Faridabad 121001, Haryana, India
[c] National Institute of Chemistry, Hajdrihova 19, 1000 Ljubljana, Slovenia
[d] Department of Environmental Sciences, Jožef Stefan Institute, Jamova Cesta 39, 1000 Ljubljana, Slovenia

ARTICLE INFO

Keywords:
Graphitic carbon nitride
Biosensor
Voltammetry
Impedance
Nanomaterials
Covid-19

ABSTRACT

The global response to COVID-19 has exposed critical gaps in rapid, ultrasensitive, and accessible diagnostic technologies, particularly in decentralised and low-resource environments. Herein, we report the development of an electrochemical biosensor designed for ultrasensitive detection of the SARS-CoV-2 spike receptor-binding domain (RBD) protein. This platform was rationally engineered nanocomposite combined with carboxylated graphitic carbon nitride (cGCN) and gold nanoparticles (AuNPs), which synergistically enhance surface reactivity, electron transfer efficiency, and biomolecular interface stability. Hybrid nanomaterials can overcome the kinetic and sensitivity barriers of traditional biosensors, and a cGCN/AuNP hybrid was fabricated on fluorine-doped tin oxide (FTO) electrodes and functionalized with in-house generated anti-RBD antibodies. Comprehensive physicochemical characterisation confirmed the successful integration and surface engineering of the composite. Using Differential Pulse Voltammetry, the sensor achieved a limit of detection (LOD) of 0.8 fM and demonstrated limit of quantification (LOQ) of 2.65 fM. This performance exceeds that of many existing SARS-CoV-2 antigen based biosensors and underscores the utility of rational nanomaterial design for high-precision point-of-care viral diagnostics. This approach is readily adaptable for detecting emerging viral pathogens and supporting future pandemic preparedness.

1. Introduction

Severe acute respiratory syndrome coronavirus 2 (SARS-CoV-2) is a highly transmissible RNA virus classified under *Beta-coronavirus genus* [1]. It has precipitated a global pandemic, with over 777 million confirmed cases and 7.1 million fatalities reported as of 2024 [2]. Affordable and accessible diagnostic tools for SARS-CoV-2 infection remain a critical challenge, particularly in developing countries. Although nucleic acid amplification tests, such as RT-PCR, remain the clinical gold standard, their reliance on centralised laboratories, skilled personnel, and complex logistics limits their scalability, particularly in low-resource settings [3]. The diagnostic bottleneck is especially problematic during the early stages of infection or in asymptomatic individuals, when timely identification is critical to containment and treatment strategies [4–6]. The viral spike (S) protein, specifically its receptor-binding domain (RBD), plays a central role in mediating host cell entry and is a validated target for both immunological and molecular diagnostics [7–11]. Direct detection of the RBD antigen offers a promising alternative to genome-based methods, enabling faster and equipment-independent readouts. However, existing antigen detection platforms frequently suffer from suboptimal sensitivity, particularly at low viral loads, which impairs their clinical utility during early infection or convalescence [12].

Electrochemical biosensors have emerged as promising alternatives owing to their affordability, portability, and user-friendliness. These devices detect biological interactions by converting them into

* Corresponding author at: Department of Environmental Sciences, Jožef Stefan Institute, Jamova Cesta 39, 1000 Ljubljana, Slovenia.
** Corresponding author at: BRIC-National Institute of Animal Biotechnology (NIAB), Hyderabad 500032, Telangana, India.
E-mail addresses: raghuraj.singh@ijs.si (R.S. Chouhan), gandhi@niab.org.in (S. Gandhi).

https://doi.org/10.1016/j.microc.2025.114455
Received 21 March 2025; Received in revised form 17 June 2025; Accepted 1 July 2025
Available online 5 July 2025

quantifiable electrical signals [13]. By employing a signal transducer to measure the electrochemical reactions occurring at the electrode surface, these sensors exhibit high selectivity even for complex biological samples. This versatility makes them suitable for a wide range of applications, including, the detection of bacteria, viruses, and other pathogens; identifying antibiotics, pesticides, and drug molecules; diagnosing cancer; monitoring environmental conditions; and tracking diseases and overall health [14]. The generated electrochemical signals typically correspond to an increase or decrease in the response measured using techniques such as differential pulse voltammetry (DPV), cyclic voltammetry (CV), square-wave voltammetry (SWV), and electrochemical impedance spectroscopy (EIS) [15].

However, traditional electrode materials often face significant limitations, such as poor electron transfer efficiency and susceptibility to fouling, which restrict their performance in complex biological matrices. To overcome these challenges, advanced strategies, such as incorporating nanomaterials, modifying recognition probes, and introducing redox labels, have been employed [16,17].

To address these constraints, we developed a nanocomposite interface that integrates carboxylated graphitic carbon nitride (cGCN) and gold nanoparticles (AuNPs) which can overcome the sensitivity and stability limitations of conventional biosensors [18–20]. Graphitic carbon nitride offers high surface area, chemical inertness, and biocompatibility; however, its poor conductivity and dispersion properties limit its application. Carboxylation introduces polar functional groups that improve aqueous stability and promote electron transport [21–23]. When combined with AuNPs, which are known for their catalytic activity, electrical conductivity, and facile bioconjugation, the resulting hybrid forms a conductive and chemically stable matrix optimised for bio electrochemical signal transduction [24]. In addition to functional materials, the electrode substrate also plays a critical role in biosensor performance. Transparent conductive oxides (TCOs) such as fluorine-doped tin oxide (FTO) are widely employed owing to their transparency, electrical conductivity, and chemical stability. FTO is a cost-effective and less toxic alternative to indium tin oxide (ITO), whose widespread adoption is limited by its high cost and environmental concerns. The advantageous properties of FTO make it a preferred substrate for supporting nanomaterials in advanced biosensing applications [25–28].

Here, we report the development of an electrochemical immunosensor for SARS-CoV-2 RBD detection based on a cGCN/AuNP nanocomposite immobilised onto fluorine-doped tin oxide (FTO) electrodes. The sensor was functionalized with high-affinity, in-house generated anti-RBD antibodies to ensure specific and sensitive antigen recognition. The structural and chemical properties of the nanocomposite were extensively characterised using advanced techniques including X-ray diffraction (XRD), X-ray photoelectron spectroscopy (XPS), UV–Vis spectroscopy, Fourier transform infrared spectroscopy (FTIR), Transmission Electron Microscopy (TEM), energy-dispersive X-ray spectroscopy (EDXS), and Scanning Electron Microscopy (SEM), confirming its robust structural and chemical integrity. In-house-generated RBD antibodies were employed as the biorecognition element, enabling the immunosensor to achieve an exceptional limit of detection (LOD) of 0.8 fM and a limit of quantification (LOQ) of 2.65 fM, with a broad linear detection range. Specific binding between RBD protein and antibody was further validated by ELISA and western blot analysis, confirming its functionality and selectivity. This biosensor offers significant advantages, including facile synthesis, high sensitivity, and excellent stability, and demonstrates superior performance compared with existing SARS-CoV-2 biosensors. Compared with existing technologies, this biosensor offers a simplified fabrication strategy, enhanced analytical performance, and potential for adaptation to detect other infectious agents, making it a compelling candidate for next-generation point-of-care diagnostics.

2. Materials and methods

2.1. Chemicals

Melamine, gold (III) chloride trihydrate ($HAuCl_4{\cdot}3H_2O$), hydrochloric acid (HCl), sulphuric acid (H_2SO_4), Tween® 20, skimmed milk powder, Freund's complete adjuvant (FCA), Triton™ X-100, sodium azide, Bradford reagent, *N*,*N*,*N*′,*N*′-tetramethylethylenediamine (TEMED), ammonium persulphate, nitric acid (HNO_3), Freund's incomplete adjuvant (FIA), and Brilliant Blue R were obtained from Sigma-Aldrich. Guanidine hydrochloride (GHC), sodium chloride (NaCl), imidazole, sodium citrate tribasic dihydrate ($C_6H_5Na_3O_7{\cdot}2H_2O$), 2-morpholineethanesulfonic acid (MES) monohydrate, sodium phosphate dibasic anhydrous (Na_2HPO_4), potassium phosphate dibasic anhydrous (K_2HPO_4), urea, and magnesium chloride ($MgCl_2$) were purchased from Sisco Research Laboratories (SRL). Nitric acid (HNO_3) was purchased from Fisher Scientific. HisPur™ Ni-NTA resin and protein A-sepharose resin were purchased from Thermo Fisher Scientific and Cytiva, respectively. The tetramethylbenzidine (TMB) substrate solution was obtained from HiMedia. Goat anti-rabbit IgG (H + L) secondary antibody was procured from Novus Biologicals. The SARS-CoV-2 RBD Ag was produced in-house following a previously reported protocol [29]. All reagents and solvents used in this study were of analytical grade and all solutions were prepared using double-distilled water.

2.2. Synthesis and characterisation of cGCN/AuNPs nanocomposite

Green synthesis of GCN nanosheets was achieved by heating 5 g of melamine monomer at 550 °C in a ceramic container. The resulting product was transferred to a separate ceramic crucible and heated in a hot-tube furnace under an optimised heating program [30]. The pale-yellow powder was then milled into a fine powder. To produce a few layers of GCN nanosheets, 3 g of the synthesised material was mixed with 20 mL of 1 M HCl and stirred for 3 h at ambient temperature. The resulting mixture was filtered using a 0.45 μm membrane and dried at 70 °C. Subsequently, 300 mg of the dried sample was resuspended in 50 mL of Milli-Q water, sonicated for 30 min, and centrifuged at 9000 rpm for 15 min. The supernatant was carefully decanted, and the suspension was transferred to a clean flask. The remaining suspension was concentrated by distillation or by using a rotary evaporator and dried overnight at 70 °C [30,31].

For carboxylation, bulk GCN was treated with concentrated HNO_3 under continuous stirring for 24 h. The acid was thoroughly removed by repeated washing with double-distilled water (ddH_2O) until the pH of the solution reached 7. The resulting pellet was dried overnight at 37 °C. The dried product was resuspended in ddH_2O at a concentration of 1 mg/mL, sonicated for 30 min, and stored at room temperature (RT) for future applications.

Gold nanoparticles (AuNPs) were synthesised using a chemical reduction method, as described previously [32]. Briefly, 10 % gold chloride solution was introduced into 100 mL of deionised water under continuous heating and stirring. Once the solution reached boiling temperature, a 1 % sodium citrate solution was gradually added. This addition triggered a distinct colour transition from pale yellow to purple, and then to wine-red, indicating the successful formation of AuNPs. Once a stable wine-red colour was achieved, heating was ceased, and the solution was stirred until it cooled to RT. To synthesise the cGCN/AuNP composite, a modified electrostatic assembly method was employed. Equal volumes of the synthesised AuNP solution and cGCN dispersion were combined and subjected to sonication using a probe sonicator, after which the mixture was allowed to settle at RT.

The synthesised nanocomposites (GCN, AuNPs, cGCN, and cGCN/AuNPs) were comprehensively characterised to assess their structural, morphological, and optical properties. For XRD and XPS the nanocomposites were drop casted on a coverslip and dried at 37 °C. XRD patterns were recorded using a PANalytical EMPYREAN diffractometer

with Cu Kα radiation (λ = 1.5406 Å), operated at 45 kV and 40 mA, in reflection mode over a 2θ range of 3–90°, employing a continuous scan mode with 41.82 s/step. XPS was performed using a monochromatic Al Kα source (hν = 1486.6 eV) operated at 75 W (15 kV, 5 mA) in spectroscopy tuning mode. A hybrid lens and slot collimator configuration were employed with a resolution setting of 40. High-resolution spectra were acquired for the C 1 s (1186.7–1209.7 eV), N 1 s (1076.7–1096.7 eV), O 1 s (943.7–961.7 eV), and Au 4f (1391.7–1411.7 eV) regions using a step size of 0.1 e*V*, sweep time of 60 s, and dwell times between 260 and 331 ms. Survey scans were collected over a wide energy range with appropriate pass energy to allow elemental identification. Charge neutralization was applied (filament current: 0.37 A, filament bias: 1 *V*, charge balance: 4 V), and quantification was carried out using the instrument's sensitivity factors and CasaXPS software [33]. The high-resolution XPS spectra were deconvoluted using a Gaussian-Lorentzian (GL30) peak shape function to achieve accurate fitting of the observed chemical states. Each component peak was analysed based on its full width at half maximum (FWHM), binding energy position, and relative area percentage. Functional group identification and chemical modifications were confirmed using FTIR on a Nicolet iS50 FT-IR spectrometer (Thermo Electron Corporation, Shanghai, China) in the wavenumber range of 4000–500 cm^{-1}. The optical properties were evaluated using a Systonic S-924 Single-Beam UV–Vis Spectrophotometre (Delhi, India) by analysing aqueous nanocomposite solutions. Morphological features and elemental compositions were studied via SEM and EDXS using Zeiss EVO-18 scanning electron microscope (Zeiss, Germany) operated at an accelerating voltage of 20 kV. A small aliquot of the nanoparticle suspension was drop-cast onto a carbon-coated copper TEM grid and allowed to dry at 37 °C. TEM was performed using a JEOL-JEM F2000 microscope (JEOL, Japan) at 200 kV to visualise the nanosheet structures and nanoparticle distributions. XRD, XPS, FTIR, and UV–Vis spectra were baseline-corrected, smoothed, and plotted, with sharp diffraction peaks fitted using GraphPad, and Origin software to ensure accurate analysis and representation of the data.

2.3. Fabrication and optimization of cGCN/AuNPs/RBD ab electrode

The electrochemical behaviour and performance of GCN, AuNPs, cGCN, and cGCN/AuNP nanocomposites on the electrodes were systematically evaluated. These analyses were performed using a Palmsens4 potentiostat (Netherlands) equipped with PS Trace software. The baseline redox behaviour of each material was examined using DPV. Bare electrodes were modified by drop-casting 1 mg/mL solutions of GCN, AuNPs, cGCN, cGCN/AuNPs (1:1 ratio), and cGCN/AuNPs functionalised with the RBD antibody (1 μg/mL). The coated electrodes were air-dried at room temperature before testing. The electrochemical stability and redox potentials of the cGCN/AuNP nanocomposites were analysed by optimising the ratio of cGCN to AuNPs, varying from 1:0.2 to 1:1. To assess the time-dependent electrochemical responses, the coated electrodes were immersed in the electrolyte for 5 min prior to measurements. The DPV scans were performed at intervals of 5, 30, 60, 90, 120, 150, and 180 s to determine the optimal response time. The effect of temperature on the current output was studied at 4, room temperature (RT), and 37 °C. Similarly, the effect of pH was evaluated over a wide range (5.0, 5.5, 6.0, 6.5, 7.0, 7.5, and 8.0). To optimise the antibody concentration on the cGCN/AuNP-coated electrode, different amounts (ranging from 0.5 to 2 μg/mL) of anti-RBD antibody were tested, and their impact on the current output was recorded. The potential range was set between −1.2 *V* and + 1.2 V, and the optimal scan rate was determined by varying it from 0.01 V/s to 0.1 V/s. The current response under each condition was recorded and plotted against the applied potential, providing insights into the redox performance, stability, and optimal operating conditions of the fabricated electrodes.

2.4. Analytical performance of cGCN/AuNPs/RBD ab electrode for RBD ag detection

The analytical performance of the c-GCN/AuNP/RBD-Ab-modified electrode for detecting the RBD antigen (RBD—Ag) over a concentration range of 10fM - 1 μM was systematically evaluated using DPV. A linear calibration curve was established by plotting the current response as a function of the logarithm of antigen concentration. A calibration curve was used to determine the limits of detection (LOD) and quantification (LOQ). These metrics were calculated using the formula LOD = [3.3 × (σ/S)] and LOQ = [10 × (σ/S)], where σ represents the standard deviation of the response (calculated from the standard error of the Y-intercept) and S corresponds to the slope of the calibration curve, following the method described in [34]. The stability of the electrodes was assessed over a 21-day period by storing them at 4 °C and recording their DPV responses at 7-day intervals to track any decline in the current output. Repeatability was evaluated by performing five consecutive DPV measurements on a single electrode at a fixed RBD-Ag concentration, and reproducibility was tested using three independently fabricated electrodes under identical conditions. The consistency of these measurements were analysed based on standard deviation (SD) values using GraphPad Prism 10 software, confirming the reliability and robustness of the electrode for detecting RBD—Ag.

3. Results and discussion

3.1. Synthesis and characterisation of GCN, cGCN, AuNPs and cGCN/AuNPs

The synthesised samples were characterised using a range of analytical techniques to determine their structural, chemical, and physical properties. The phase composition was examined using XRD, which provided insight into the crystalline structures and interlayer arrangements. The characteristic peaks observed at 12.8° and 27.2° (2θ) were attributed to the tris-*s*-triazine interlayer stacking (001) and the in-plane structural motif of the conjugated aromatic rings (002), as shown in Fig. 1(a, c, d) [30]. These peaks confirm the characteristic stacking structures of the GCN, cGCN, and cGCN/AuNP nanocomposites. Additionally, the XRD patterns in Fig. 1(b) and (d) display four distinct peaks at 38.1°, 44.3°, 64.5°, and 77.7° (2θ), corresponding to the (111), (200), (220), and (311) crystallographic planes, respectively. These peaks indicate a face-centred cubic (fcc) crystalline structure, consistent with the standard Bragg diffraction for gold. The prominent diffraction peak at 38.1° suggests a preferred growth orientation along the (111) plane for zero-valent gold, indicating that the nanostructure was stabilised during the synthesis [35]. The different peaks of the cGCN/AuNP nanocomposite spectra corresponding to AuNPs indicated successful loading in the cGCN nanosheets.

XPS was used to analyse the chemical composition of the cGCN/AuNP nanocomposites. The XPS profiles, shown in Fig. 1(f g), reveal prominent C1s (~285 eV) and N1s (~400 eV) peaks, which correspond to the primary building blocks of GCN, cGCN, and cGCN/AuNPs [30]. In Fig. 1(e and h), a small O1s (~530 eV) peak is likely due to adsorbed atmospheric H_2O or CO_2 during the preparation of GCN samples [36]. For AuNPs alone, Fig. 1(i) exhibits clear signals for Au4f (~ 90 eV), C1s, and O1s, confirming that the gold nanoparticles were stabilised and capped with citrate. Fig. 1(m) demonstrated an increased intensity of C1s and O1s peaks in the cGCN sample, validating the successful carboxylation process [37]. In the cGCN/AuNP nanocomposite (Fig. 1q), the presence of C1s, N1s, O1s, and Auf4 peaks confirmed the successful integration of both nanomaterials, highlighting their compatibility and effective hybridisation. These results demonstrate that the essential features of GCN are retained following carboxylation and hybridisation with AuNPs. In the high-resolution spectra, GCN (Fig. 1f, g, and h), AuNPs (Fig. 1j, k, and l), cGCN (Fig. 1n, o, and p), and cGCN/AuNP (Fig. 1r, s, t, and u) exhibit distinct chemical signatures corresponding to

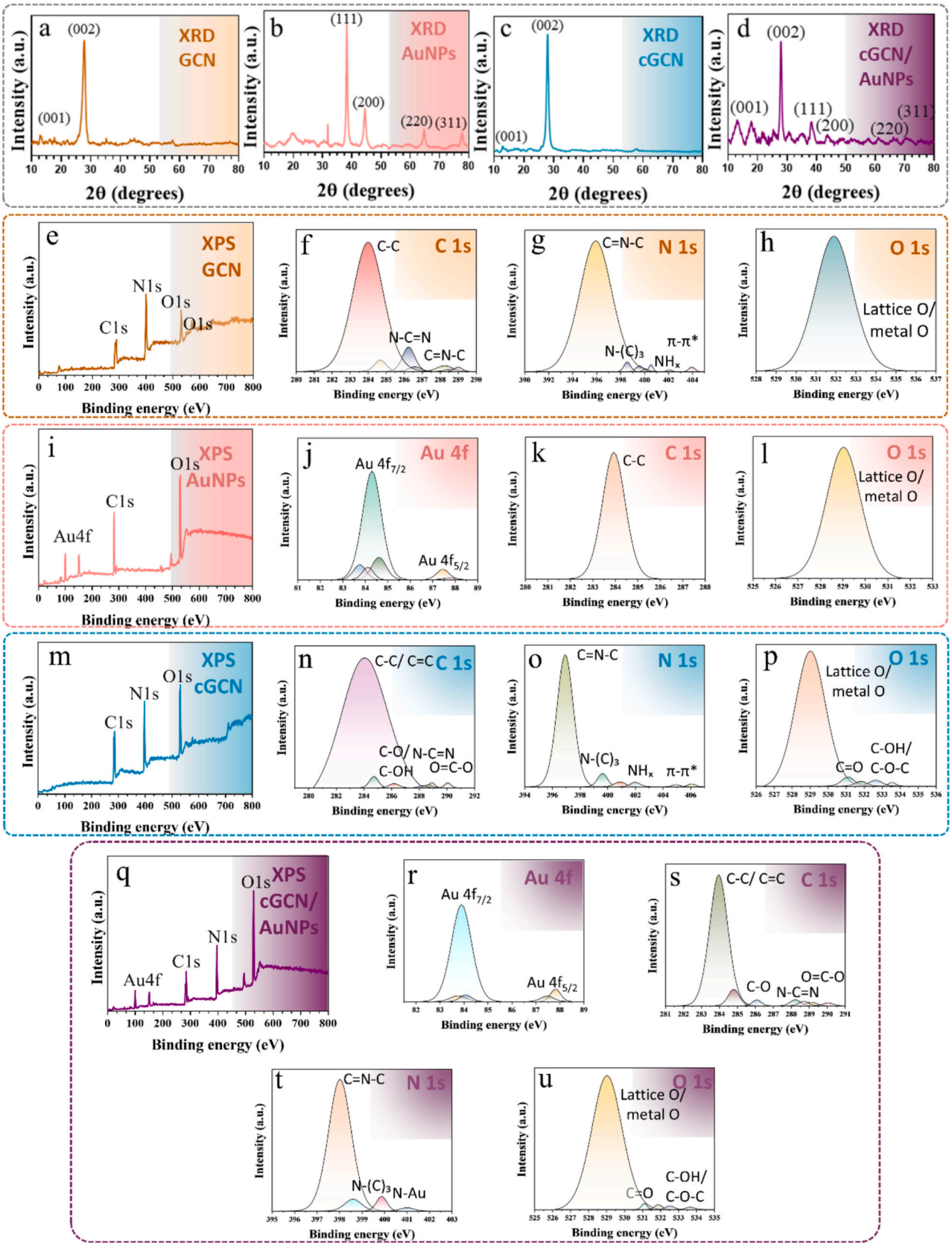

Fig. 1. Crystalline and elemental properties of GCN, AuNPs, cGCN, and cGCN/AuNP nanocomposites. (a-d) XRD patterns of (a) GCN, (b) AuNPs, (c) cGCN, and (d) cGCN/AuNPs, highlighting the characteristic peaks that confirm the structural integrity of the materials. (e-h) X-ray Photoelectron Spectroscopy (XPS) spectra of (e) GCN, (i) AuNPs, (m) cGCN, and (q) cGCN/AuNPs revealing the surface elemental properties of each sample. High-resolution XPS spectra of core-level regions for (f-h) GCN, (j-l) AuNPs, (n-p) cGCN, and (r–u) cGCN/AuNP nanocomposite. The deconvoluted peaks in the N 1 s, C 1 s, O 1 s, and Au 4f regions reflect changes in chemical bonding environments during each stage of nanocomposite preparation.

their respective elemental compositions and surface modifications, as evidenced by the shifts and intensity variations in the N 1 s, C 1 s, O 1 s, and Au 4f regions.

FTIR analysis of GCN, AuNPs, cGCN, and the cGCN/AuNP nanocomposites revealed characteristic vibrational fingerprints corresponding to N–H/O–H bonds, tri-*s*-triazine units, and C=N/C–N units (Fig. S1). Broad absorption bands around 3240–3500 cm^{-1} were attributed to N–H/O–H stretching vibrations, observed in GCN, cGCN, and cGCN/AuNPs, consistent and aligned with the previously reported studies [38].The distinct peak at 1642 cm^{-1} was assigned to the amide groups, suggesting the presence of residual amine functionalities. The notable peak at 806 cm^{-1} was attributed to the out-of-plane bending vibrations of the heptazine ring, which is a signature feature of the tri-*s*-triazine units in the GCN structure. Meanwhile, a broad absorption band in the range of 1147–1632 cm^{-1} corresponded to vibrations linked to by-products of the tri-*s*-triazine framework observed in GCN, cGCN, and cGCN/AuNPs [39]. Following the carboxylation of GCN, new peaks appeared at 1734 cm^{-1}, corresponding to C=O bending vibrations, along with peaks at 1569 cm^{-1} and 1322 cm^{-1}, attributed to -COO^{-} absorption bands. These features confirm the successful carboxylation of the GCN nanosheets, demonstrating the structural modifications necessary for enhanced functionalisation and integration into the cGCN/AuNP nanocomposite (Fig. S1).

The morphological and elemental compositions of GCN, AuNPs, cGCN, and cGCN/AuNP nanocomposites were analysed using SEM and EDXS, as illustrated in Fig. 2 (a-h). The SEM images in Fig. 2((a), (c), (e), and (g)) reveal significant differences in the structural morphologies of the samples. Fig. 2(a) displays the layered and stacked morphology typical of pristine GCN nanosheets [40], whereas Fig. 2(c) depicts spherical nanoparticles with a uniform distribution, which is characteristic of AuNPs [41]. In Fig. 2(e), the cGCN exhibits a rough and more fragmented surface than GCN, which might be the result of inductive

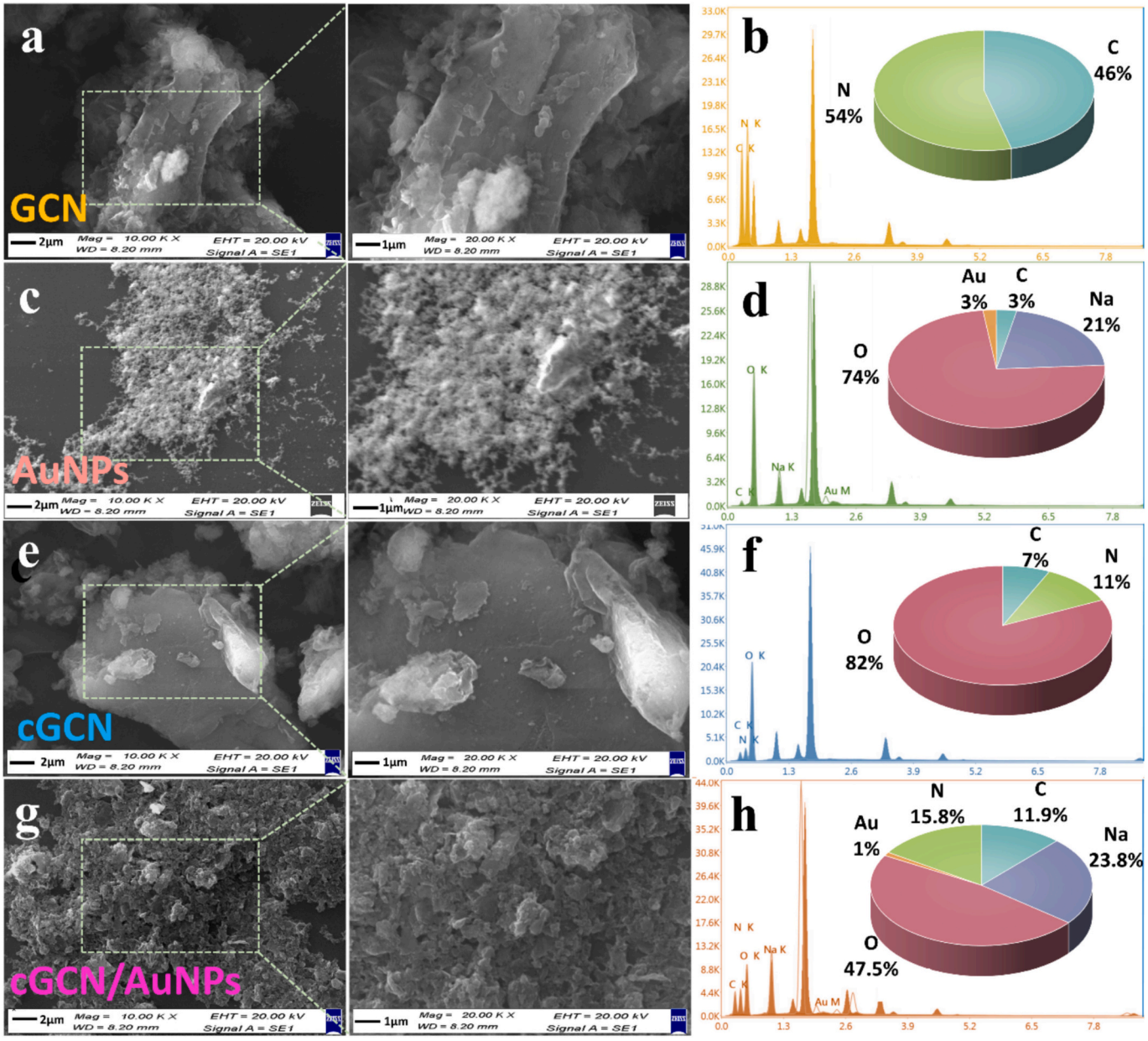

Fig. 2. Morphological and compositional characterisation of GCN, AuNPs, cGCN, and the cGCN/AuNPs composite. (a, c, e, g) SEM images of GCN, AuNPs, cGCN, and cGCN/AuNP composites. (b, d, f, h) Corresponding EDXS spectra and elemental composition analysis of GCN, AuNPs, cGCN, and cGCN/AuNP composites, respectively.

surface functionalization. The c-GCN/AuNP composite in Fig. 2(g) demonstrated the effective integration and intercalation of AuNPs onto the cGCN surface, forming a rough and porous nanocomposite structure.

The EDXS analysis shown in Fig. 2b, d, f, and h confirm the elemental composition of the bare and nanocomposite materials. For GCN, Fig. 2 (b), 46 % carbon and 54 % nitrogen were the predominant elements, consistent with its graphitic structure [40]. The EDXS spectrum of AuNPs Fig. 2(d) indicates the presence of gold, along with minor amounts of carbon (3 %), Na (21 %), and oxygen (74 %), which may result from the citrate capping agent [41]. The cGCN spectrum in Fig. 2 (f) shows an increased oxygen signal (~82 %), confirming the introduction of carboxyl groups during carboxylation. The c-GCN/AuNP spectrum shown in Fig. 2(h) highlights the presence of 11.9 % carbon, 15.8 % nitrogen, 47.5 % oxygen, 23.8 % Na, and 1 % gold, further validating the successful integration of AuNPs into the cGCN matrix. The elemental mapping analysis (Fig. S2) provided further visualization of

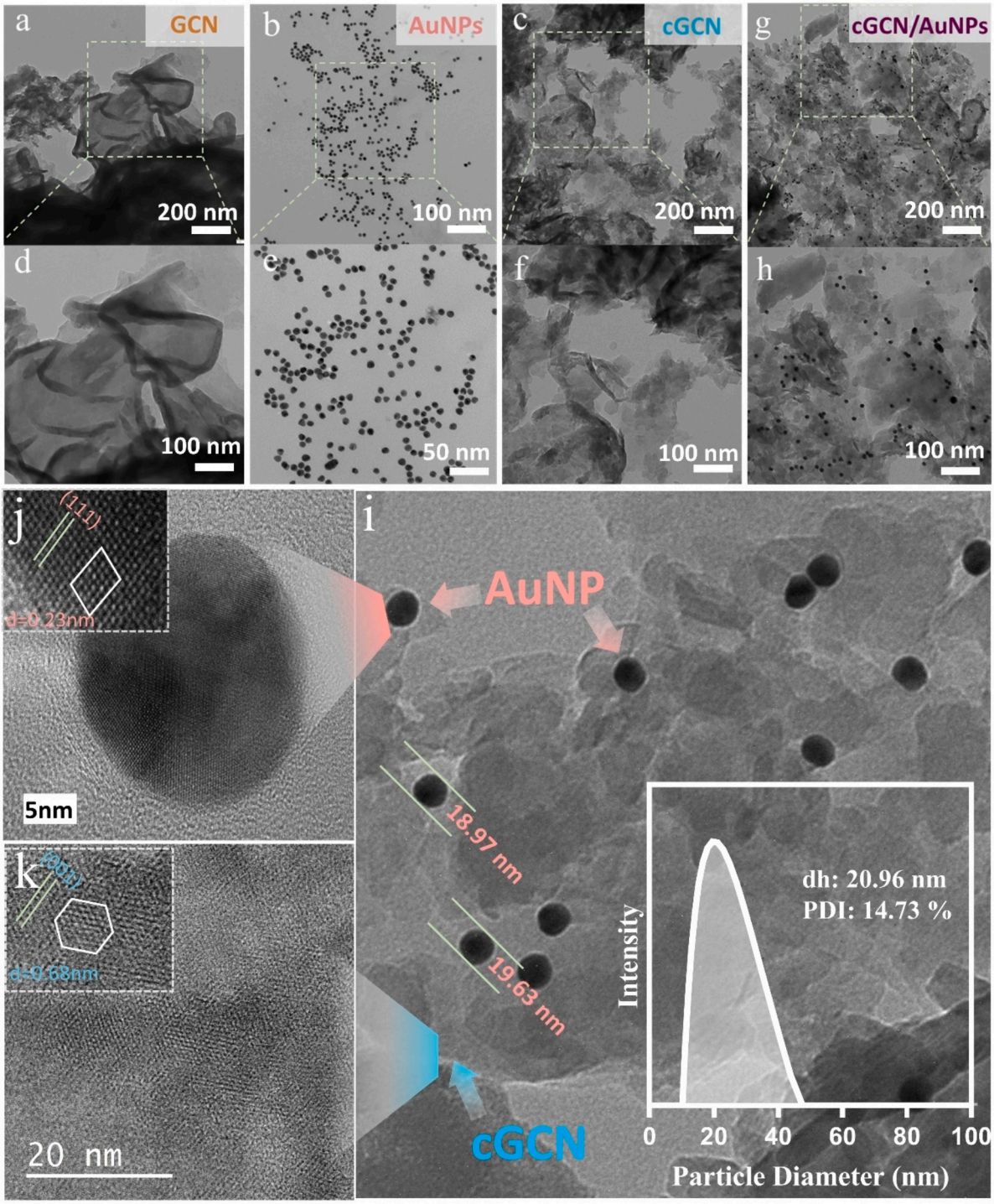

Fig. 3. TEM images of GCN, AuNPs, cGCN, and the composite material cGCN/AuNPs. (a and d) TEM images of GCN. (b and e) TEM images of AuNPs. (c and f) TEM images of cGCN. (g and h) TEM images of cGCN/AuNP composites. (i) TEM image of the cGCN/AuNP composite showing the interface between AuNPs and cGCN with an inset of size distribution of AuNPs with polydispersity index of 14.73 % and dynamic diameter of 20.96 nm. High-resolution transmission electron microscopy (HR-TEM) of AuNP (j) and cGCN (k).

the elemental distribution within each nanomaterial. The uniform distribution of carbon and nitrogen in GCN, localised gold signal in AuNPs, and combined distribution of carbon, nitrogen, and gold in the cGCN/AuNP composite further corroborated the successful synthesis and integration of these nanomaterials.

Transmission electron microscopy (TEM) analysis provided detailed insights into the structural features of the synthesised materials. The GCN displayed a stacked, blanket-like arrangement composed of well-distributed slices that resembled randomly oriented graphene-like layers with a smooth surface (Fig. 3a, d). The spherical morphology of the colloidal AuNPs was confirmed by TEM imaging, which revealed the presence of nanoparticles with an average diameter of 19 ± 5 nm (Fig. 3b, e, g, h, i). In the case of cGCN, the TEM images showed a more compact structure with enhanced porosity compared to pristine GCN, likely due to the carboxylation process (Fig. 3c, f, g, h, i). TEM analysis of the cGCN/AuNP nanocomposite demonstrated a uniform distribution of AuNPs on the cGCN sheets, which appeared to be more symmetrical in size. This structural uniformity may have resulted from the cutting effect introduced during the synthesis process (Fig. 3g, h, i). Collectively, these results validated the successful fabrication of the cGCN/AuNP nanocomposite while retaining the structural integrity of the individual components. HR-TEM images confirm the lattice fringes corresponding to the (001) plane of GCN with a d spacing of 6.8 A° and the (111) plane of Au with a d spacing of 2.3 A°, indicating high crystallinity (Fig. 3j and k).

3.2. Characterisation of RBD Ag and RBD Ab for the fabrication of electrode

The RBD of SARS-CoV-2 spike protein plays a critical role in viral infection by binding to the angiotensin-converting enzyme 2 (ACE2) receptor on host cells. To characterise the recombinant RBD antigen and in-house produced anti-RBD antibody, a series of analytical techniques were employed. SDS-PAGE analysis of the purified RBD antigen revealed a distinct band at approximately 31 kDa, which is consistent with the expected molecular weight (Fig. S3a). Similarly, SDS-PAGE analysis of the purified RBD antibody revealed two clear bands at approximately 50 kDa and 25 kDa, corresponding to the heavy and light chains, respectively (Fig. S3b). The identity and purity of the RBD antigen were further confirmed by western blot analysis, which showed a strong, specific band at 31 kDa when probed with the RBD antibody generated in-house (Fig. S3c). To assess the interaction between the RBD antigen and RBD antibody, a binding assay was performed, which demonstrated a concentration-dependent increase in absorbance at 450 nm. The results identified 5 μg/mL antigen and 10 μg/mL antibody as the optimal concentrations for interaction, indicating a robust and specific binding between the two (Fig. S3d). These results collectively validate the successful production, purification, and detailed characterisation of both the RBD antigen and RBD antibody, confirming their suitability for further experimental applications.

3.3. Electrode fabrication, optimization and characterisation of cGCN/AuNPs/RBD-ab

The electrochemical characterisation of the fabricated sensor was performed using DPV, and a comprehensive evaluation of the factors influencing the sensor performance is shown in Fig. S4 (a-f). The stepwise assembly of the sensing interface was monitored via sequential DPV measurements. Each modification stage resulted in a marked increase in the peak current compared to the bare electrode, which was attributed to the improved electron transfer kinetics facilitated by the addition of conductive nanomaterials. Upon antibody immobilisation, a distinct decrease in current was observed, indicating a reduced electroactive surface area due to biomolecular coverage, consistent with successful immobilisation of the biorecognition element and suppression of surface electron transfer (Fig. S4a). Optimisation of the nanocomposite ratio revealed that a 1:1 mass ratio of cGCN to AuNPs produced the highest peak current, confirming a synergistic interaction at this specific composition. This balance appears to optimise the electrical conductivity of the interface while preserving adequate surface functionality for antibody binding, thereby facilitating efficient signal transduction (Fig. S4b). The sensor exhibited a rapid response time, reaching a stable peak current signal within 30 s, which is crucial for real-time monitoring (Fig. S4c). Temperature optimisation showed that the peak current was maximised at 25 °C, reflecting an optimal balance between antibody activity and reaction kinetics under physiological conditions. A decrease in the signal was observed at higher temperatures (for example, 37 °C), likely due to partial denaturation or conformational changes of the antibody, whereas lower temperatures (for example, 4 °C) led to suppressed kinetics and limited analyte diffusion (Fig. S4d). The pH plays a critical role in maintaining the structural and functional integrity of the immobilised antibodies, as well as in modulating the charge distribution at the electrode interface. At physiological pH (~7.0), the antibodies retained their native conformation and optimal binding affinity toward the SARS-CoV-2 RBD antigen, resulting in efficient recognition and electron transfer. Deviation from neutral pH leads to altered protonation states of both the electrode surface and biomolecules, disrupting the antigen–antibody interaction and thereby reducing the current response. Under acidic conditions, excess protons may interfere with the electrochemical double layer and suppress the redox activity. In alkaline media, the deprotonation of surface functional groups and denaturation of protein structures can impair both binding efficiency and signal stability. Furthermore, extreme pH conditions may alter the local ionic strength and dielectric properties of the medium, impeding the overall kinetics of electron transfer at the cGCN/AuNP-modified electrode surface. These factors collectively contributed to the suboptimal performance observed at pH values lower or higher than 7 (Fig. S4e). The antibody immobilisation concentration was also evaluated, with 1 μg/mL yielding the highest peak current, suggesting saturation of the available binding sites and maximal capture efficiency at this concentration. Higher concentrations did not improve the signal intensity, likely because of steric hindrance or multilayer formation that impeded electron transfer (Fig. S4f). The scan rate was evaluated within the range of 0.01 *V*/s to 0.1 V/s, revealing a proportional increase in peak current as the scan rate increased. This relationship was further validated through linear regression analysis, which showed a significant *p*-value (<0.0001) and an R^2 value of 0.9780, with the maximum current observed at a scan rate of 0.1 V/s (Fig. S5). These results validate the effective fabrication and optimisation of an electrochemical sensor with high sensitivity and specificity for the detection of SARS-CoV-2.

3.4. Analytical performance of cGCN/AuNPs/RBD-Ab electrodes

The analytical performance of cGCN/AuNP/RBD–Ab immunosensor was assessed using DPV. A reduction in the current was observed as the concentration of SARS-CoV-2 RBD antigen increased, ranging from 10 fM to 1 μM (Fig. 4a). This reduction in conductivity was attributed to the formation of an antigen layer on the electrode surface, which decreased the conductive area and impeded electron transfer. This reduction in conductivity can be attributed to a protein-masking effect, where the antigen layer obstructs the electron flow. A standard linear calibration curve was constructed by plotting the peak current against the logarithm of antigen concentration. The curve exhibited a strong correlation with a significant p-value (<0.0001), slope of −115.8, intercept of 28.08, and R^2 value of 0.9507. The LOD of the fabricated electrode was determined to be 0.8 fM. Similarly, LOQ = [10 × (σ/S)] yielded a value of 2.65 fM (Fig. 4a). These results confirm the high sensitivity and analytical efficiency of the sensor.

Stability is a critical factor for validating the performance of a biosensor. The stability of the cGCN/AuNP/RBD-Ab electrode was evaluated for 3-weeks at 4 °C. While antibody activity remained unaffected for up to 7 days, a noticeable decline in output current was

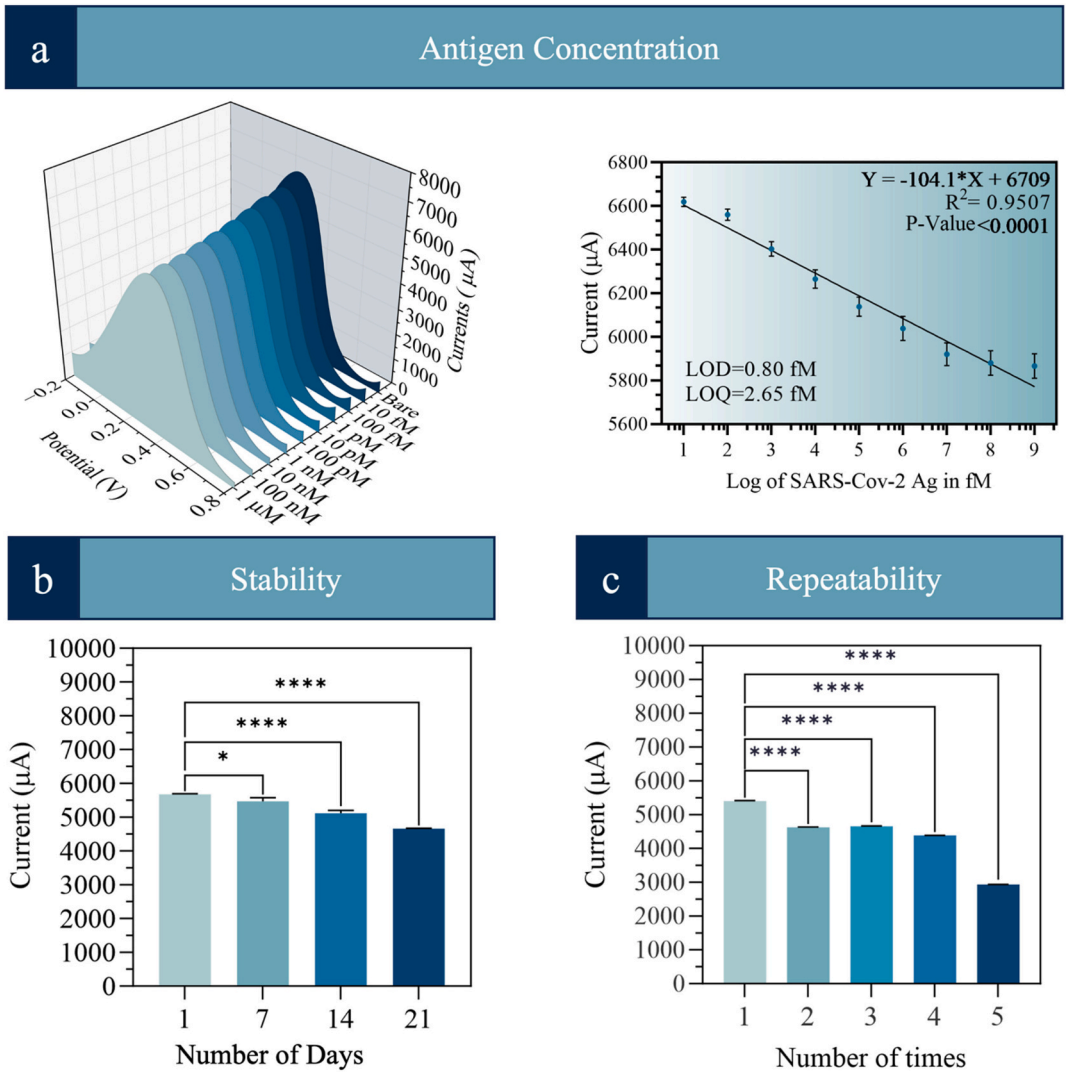

Fig. 4. Analytical performance of the fabricated electrochemical immunosensor. (a) Calibration curve showing the sensor response to varying concentrations of the SARS-CoV-2 antigen. The LOD and LOQ are 0.8 fM and 2.65 fM. (b) Evaluation of sensor stability over a 21-day period. (c) Assessment of the sensor repeatability across five independent measurements. (All Data are presented as mean ± SD, with $n = 3$. Statistical significance is indicated as $^{*}p < 0.05$ and $^{****}p < 0.0001$ compared to the respective control using a one-way ANOVA test).

observed at weekly intervals, indicating a gradual reduction in electrode efficacy over time. This suggests that although stable in the short term, the performance of the electrode diminished with prolonged storage (Fig. 4b). In addition, the reusability of the electrode was tested through five consecutive measurements using individual sensors. The results demonstrated that cGCN/AuNP/RBD-Ab electrodes could be effectively used up to four time without significant performance loss. (Fig. 4c). Table 1 showed the comparative analysis of electrochemical biosensors developed for SARS-CoV-2 protein detection.

4. Conclusions

This study presents a nanostructured electrochemical immunosensor that addresses the key limitations in SARS-CoV-2 antigen detection by integrating carboxylated graphitic carbon nitride (cGCN) with gold nanoparticles (AuNPs). The cGCN/AuNP composite demonstrated enhanced conductivity, surface reactivity, and biofunctional integration to overcome the challenges of signal instability and low sensitivity of conventional sensing interfaces. The analytical performance of the sensor was evaluated using differential pulse voltammetry (DPV), demonstrating an ultralow limit of detection of 0.8 fM and a limit of quantification of 2.65 fM, with a broad linear dynamic range. These results represent a significant improvement over many previously reported SARS-CoV-2 biosensors, highlighting the platform's exceptional sensitivity and signal resolution. The sensor exhibited excellent reproducibility, operational stability, and reusability over multiple measurement cycles and storage periods. This work demonstrates not only the diagnostic promise of the developed SARS-CoV-2 biosensor but also the broader potential of cGCN/AuNP-based interfaces for detecting other viral antigens. The adaptability, high sensitivity, and robustness of the platform position are valuable tools for pandemic preparedness and infectious disease surveillance incorporating the standard addition technique in future investigations will further refine analytical performance, particularly in complex clinical environments. These findings provide meaningful insights into the development of nanomaterial-enabled electrochemical biosensors for global health applications.

Funding statement and Acknowledgements

The authors acknowledge the research endowment under the Intensification of Research in High Priority Area (IRHPA) program from the Science and Engineering Research Board (SERB), New Delhi (Grant

Table 1
Comparative analysis of electrochemical biosensors for SARS-CoV-2 protein detection.

Sl No	Type	Target	Limit of Detection	Reference
1	Bi_2WO_6/Bi_2S_3 and g-C_3N_4/Au/WO_3 Immunosensor	Nucleocapsid protein	3 fg/mL	[42]
2	GC/rGO-EDC-NHS/Ab/BSA electrode impedimetric immunosensor	S-protein RBD	150 ng/mL	[43]
3	GNPs@MUA/anti-RBD antibodies	S-protein RBD	0.577 pg/mL	[44]
4	SiO_2@UiO-66 nanocomposite Immunosensor	S-protein	100.0 fg/mL	[45]
5	SARS-CoV-2 SP anti-SARS-CoV-2/EDA-GCF electrodes in $[Fe(CN)_6]^{3-/4-}$ solution	S-protein	25 pg/mL	[46]
6	Screen-printed carbon electrode (SPCE) with nickel hydroxide nanoparticles (Ni$(OH)_2$ NPs)	S-protein	0.3 fg/mL	[47]
7	Bare GE + S1Ab + S1 protein	S-protein	15 ng/mL	[48]
	Screen-printed carbon electrode modified (SPCE) with Cu_2O nanocubes (Cu_2O NCs)	S-protein	0.04 fg/mL	[49]
8	Electrochemical biosensor using a highly uniform Au micropattern	S-protein	276 fM	[50]
9	SPCE/AuNPs/MAA/EDC-NHS/antibody/BSA/antigen Immunosensor	S-protein	3.16 pM	[51]
10	Anti-SP immobilised AuIDE Immunosensor	S-protein	189 fM	[52]
11	Boron doped diamond (BDD)-based impedimetric sensor	S-protein	1 fg/mL	[53]
12	MB-based SPEs and a portable potentiostat	S-protein	0.54 ng/mL	[54]
13	Polypyrrole-based MIP (MIP-Ppy)	S-protein	–	[55]
14	MIP-Ppy modified Pt electrode	S-protein	–	[56]
15	cGCN/AuNPs/anti-RBD based electrochemical immunosensor	S-protein RBD	0.80 fM	Present study

Number IPA/2020/000069). The Slovenian Research Agency is acknowledged for funding projects J7–60123, J13033, BI-US/22–24-162, BI-LV/25–27-004, and P1–0143. Ramya P R would like to acknowledge DBT Fellowship (DBT/2022–23/NIAB/2051) provided by the Department of Biotechnology (DBT), New Delhi.

CRediT authorship contribution statement

P.R. Ramya: Writing – review & editing, Writing – original draft, Methodology, Investigation, Formal analysis. **Shivmuni Sarup:** Writing – review & editing, Investigation, Formal analysis. **Ivan Jerman:** Writing – review & editing, Methodology, Investigation. **Raghuraj Singh Chouhan:** Writing – review & editing, Visualization, Funding acquisition, Conceptualization. **Sonu Gandhi:** Visualization, Supervision, Project administration, Funding acquisition, Conceptualization.

Ethics approval statement

All cloning and biosafety experiments were performed at the National Institute of Animal Biotechnology (NIAB), Hyderabad, after approval from the Institutional Biosafety Committee (IBSC-IBSC/May2020/NIAB/SG-01). All animal experiments were conducted at the Small Animal Facility, National Institute of Animal Biotechnology (NIAB), Hyderabad, after obtaining approval from the Institutional Animal Ethics Committee (IAEC/NIAB/2023/46/SG).

Declaration of competing interest

The authors declare that they have no known competing financial interests or personal relationships that could have appeared to influence the work reported in this paper.

Appendix A. Supplementary data

Supplementary data to this article can be found online at https://doi.org/10.1016/j.microc.2025.114455.

Data availability

The data that support the findings of this study are available from the corresponding author upon reasonable request owing to privacy/ethical restrictions.

References

[1] M. Magnen, R. You, A.A. Rao, R.T. Davis, L. Rodriguez, O. Bernard, C.R. Simoneau, L. Hysenaj, K.H. Hu, M. Maishan, C. Conrad, O.M. Gbenedio, B. Samad, C. Love, P. G. Woodruff, D.J. Erle, C.M. Hendrickson, C.S. Calfee, M.A. Matthay, J.P. Roose, A. Sil, M. Ott, C.R. Langelier, M.F. Krummel, M.R. Looney, Immediate myeloid depot for SARS-CoV- 2 in the human lung, Sci. Adv. 10 (2024), https://doi.org/10.1126/SCIADV.ADM8836.
[2] COVID-19 deaths reported (2024 global), (n.d.). https://data.who.int/dashboards/covid19/circulation?n=o (accessed November 12, 2024).
[3] A. Tharak, B. Asritha, S. Venkata Mohan, Electrochemical signatures as a diagnostic tool for SARS-CoV-2 and its variant detection in real-time wastewater samples, ACS EST Water 4 (2024) 4474–4485, https://doi.org/10.1021/ACSESTWATER.4C00468.
[4] D. Griffiths, G. Hall, Biosensors — what real progress is being made? Trends Biotechnol. 11 (1993) 122–130, https://doi.org/10.1016/0167-7799(93)90086-O.
[5] P.R. Ramya, S. Halder, K. Nagamani, R. Singh Chouhan, S. Gandhi, Disposable graphene-oxide screen-printed electrode integrated with portable device for detection of SARS-CoV-2 in clinical samples, Bioelectrochemistry 158 (2024) 108722, https://doi.org/10.1016/j.bioelechem.2024.108722.
[6] M.L. Yola, Sensitive sandwich-type voltammetric immunosensor for breast cancer biomarker HER2 detection based on gold nanoparticles decorated cu-MOF and Cu2ZnSnS4 NPs/Pt/g-C3N4 composite, Microchim. Acta 188 (2021) 78, https://doi.org/10.1007/s00604-021-04735-y.
[7] L. Premkumar, B. Segovia-Chumbez, R. Jadi, D.R. Martinez, R. Raut, A. J. Markmann, C. Cornaby, L. Bartelt, S. Weiss, Y. Park, C.E. Edwards, E. Weimer, E. M. Scherer, N. Rouphael, S. Edupuganti, D. Weiskopf, L.V. Tse, Y.J. Hou, D. Margolis, A. Sette, M.H. Collins, J. Schmitz, R.S. Baric, A.M. de Silva, The receptor-binding domain of the viral spike protein is an immunodominant and highly specific target of antibodies in SARS-CoV-2 patients, Sci Immunol 5 (2020) eabc8413, https://doi.org/10.1126/SCIIMMUNOL.ABC8413.
[8] W. Tai, L. He, X. Zhang, J. Pu, D. Voronin, S. Jiang, Y. Zhou, L. Du, Characterization of the receptor-binding domain (RBD) of 2019 Novel coronavirus: implication for development of RBD protein as a viral attachment inhibitor and vaccine, Cellular Mol. Immunol. 17 (2020) 613–620, https://doi.org/10.1038/s41423-020-0400-4.
[9] R. Ahirwar, S. Gandhi, K. Komal, G. Dhaniya, P.P. Tripathi, V.M. Shingatgeri, K. Kumar, J.G. Sharma, S. Kumar, Biochemical composition, transmission and diagnosis of SARS-CoV-2, Biosci. Rep. 41 (2021) BSR20211238, https://doi.org/10.1042/BSR20211238.
[10] N.S. Shrikrishna, S. Halder, V. Kesarwani, K. Nagamani, S. Gandhi, Unveiling the potential: high-affinity aptamers for point of care detection of SARS-CoV-2 RBD protein and it's validation in clinical samples, Chem. Eng. J. 493 (2024) 152841, https://doi.org/10.1016/j.cej.2024.152841.
[11] C.N. Botelho, S.S. Falcão, R.-E.P. Soares, S.R. Pereira, A.S. de Menezes, L.T. Kubota, F.S. Damos, R.C.S. Luz, Evaluation of a photoelectrochemical platform based on strontium titanate, sulfur doped carbon nitride and palladium nanoparticles for detection of SARS-CoV-2 spike glycoprotein S1, Biosens Bioelectron X 11 (2022) 100167, https://doi.org/10.1016/j.biosx.2022.100167.
[12] F.T. Aboagye, L. Annison, H.K. Hackman, M.E. Acquah, Y. Ashong, I. Owusu-Frimpong, B.C. Egyam, S. Annison, G. Osei-Adjei, S. Antwi-Baffour, Comparative evaluation of RT-PCR and antigen-based rapid diagnostic tests (ag-RDTs) for SARS-CoV-2 detection: performance, variant specificity, and clinical implications, Microbiol Spectr 12 (2024) e00073, https://doi.org/10.1128/SPECTRUM.00073-24.
[13] N.J. Ronkainen, H.B. Halsall, W.R. Heineman, Electrochemical biosensors, Chem. Soc. Rev. 39 (2010) 1747–1763, https://doi.org/10.1039/B714449K.
[14] S. Islam, S. Shukla, V.K. Bajpai, Y.-K. Han, Y.S. Huh, A. Kumar, A. Ghosh, S. Gandhi, A smart nanosensor for the detection of human immunodeficiency virus and associated cardiovascular and arthritis diseases using functionalized graphene-

based transistors, Biosens. Bioelectron. 126 (2019) 792–799, https://doi.org/10.1016/j.bios.2018.11.041.
[15] F.H. Pilz, P. Kielb, Cyclic voltammetry, square wave voltammetry or electrochemical impedance spectroscopy?Interrogating electrochemical approaches for the determination of electron transfer rates of immobilized redox proteins, BBA Advances 4 (2023) 100095, https://doi.org/10.1016/j.bbadva.2023.100095.
[16] A. Barhoum, S. Hamimed, H. Slimi, A. Othmani, F.M. Abdel-Haleem, M. Bechelany, Modern designs of electrochemical sensor platforms for environmental analyses: principles, nanofabrication opportunities, and challenges, Trends in Environmental Analytical Chemistry 38 (2023) e00199, https://doi.org/10.1016/j.teac.2023.e00199.
[17] C. Karaman, O. Karaman, N. Atar, M.L. Yola, Electrochemical immunosensor development based on core-shell high-crystalline graphitic carbon nitride@carbon dots and Cd0.5Zn0.5S/d-Ti3C2Tx MXene composite for heart-type fatty acid–binding protein detection, Microchim. Acta 188 (2021) 182, https://doi.org/10.1007/s00604-021-04838-6.
[18] V. Hasija, S. Patial, P. Singh, V.-H. Nguyen, Q. Van Le, V.K. Thakur, C.M. Hussain, R. Selvasembian, C.-W. Huang, S. Thakur, P. Raizada, Photocatalytic inactivation of viruses using graphitic carbon nitride-based photocatalysts: virucidal performance and mechanism, Catalysts 11 (2021) 1448, https://doi.org/10.3390/catal11121448.
[19] M. Benedet, G. Andrea Rizzi, A. Gasparotto, O.I. Lebedev, L. Girardi, C. Maccato, D. Barreca, Tailoring oxygen evolution performances of carbon nitride systems fabricated by electrophoresis through ag and au plasma functionalization, Chem. Eng. J. 448 (2022) 137645, https://doi.org/10.1016/j.cej.2022.137645.
[20] H.A. Deveci, M. Mavioğlu Kaya, İ. Kaya, B. Bankoğlu Yola, N. Atar, M.L. Yola, Bisphenol a imprinted electrochemical sensor based on graphene quantum dots with boron functionalized g-C3N4 in food samples, Biosensors (Basel) 13 (2023) 725, https://doi.org/10.3390/bios13070725.
[21] M. Amouzadeh Tabrizi, L. Nazari, P. Acedo, A photo-electrochemical aptasensor for the determination of severe acute respiratory syndrome coronavirus 2 receptor-binding domain by using graphitic carbon nitride-cadmium sulfide quantum dots nanocomposite, Sensors Actuators B Chem. 345 (2021) 130377, https://doi.org/10.1016/j.snb.2021.130377.
[22] M. Benedet, G. Andrea Rizzi, A. Gasparotto, N. Gauquelin, A. Orekhov, J. Verbeeck, C. Maccato, D. Barreca, Functionalization of graphitic carbon nitride systems by cobalt and cobalt-iron oxides boosts solar water oxidation performances, Appl. Surf. Sci. 618 (2023) 156652, https://doi.org/10.1016/j.apsusc.2023.156652.
[23] E. Scattolin, M. Benedet, D. Barreca, G.A. Rizzi, A. Gasparotto, C. Maccato, Graphitic carbon nitride functionalized with NiO nanoaggregates: an X-ray photoelectron spectroscopy investigation, Surf. Sci. Spectra 31 (2024) 024001, https://doi.org/10.1116/6.0003732.
[24] Y.-C. Yeh, B. Creran, V.M. Rotello, Gold nanoparticles: preparation, properties, and applications in bionanotechnology, Nanoscale 4 (2012) 1871–1880, https://doi.org/10.1039/C1NR11188D.
[25] A. Roberts, S. Mahari, D. Shahdeo, S. Gandhi, Label-free detection of SARS-CoV-2 spike S1 antigen triggered by electroactive gold nanoparticles on antibody coated fluorine-doped tin oxide (FTO) electrode, Anal. Chim. Acta 1188 (2021) 339207, https://doi.org/10.1016/J.ACA.2021.339207.
[26] A. Roberts, P.P. Tripathi, S. Gandhi, Graphene nanosheets as an electric mediator for ultrafast sensing of urokinase plasminogen activator receptor-a biomarker of cancer, Biosens. Bioelectron. 141 (2019) 111398, https://doi.org/10.1016/J.BIOS.2019.111398.
[27] N.S. Shrikrishna, P. Kolhe, S. Gandhi, Sensitive detection of monocrotophos using a voltametric immunosensor with randomly layered graphene oxide (GO) on fabricated electrode, J. Environ. Chem. Eng. 12 (2024) 112059, https://doi.org/10.1016/J.JECE.2024.112059.
[28] M. Shah, P. Kolhe, S. Gandhi, Two-dimensional layered MoSe2/graphene oxide (GO) nanohybrid coupled with the specific immune-recognition element for rapid detection of endosulfan, Environ. Res. 238 (2023) 117127, https://doi.org/10.1016/J.ENVRES.2023.117127.
[29] D. Shahdeo, N. Chauhan, A. Majumdar, A. Ghosh, S. Gandhi, Graphene-based field-effect transistor for ultrasensitive Immunosensing of SARS-CoV-2 spike S1 antigen, ACS Appl. Bio Mater. 5 (2022) 3563–3572, https://doi.org/10.1021/ACSABM.2C00503.
[30] R.S. Chouhan, J. Gačnik, I. Živković, S. Vijayakumaran Nair, N. Van de Velde, A. Vesel, P. Šket, S. Gandhi, I. Jerman, M. Horvat, Green synthesis of a magnetite/graphitic carbon nitride 2D nanocomposite for efficient hg $^{2+}$ remediation, environ sci, Nano 10 (2023) 2658–2671, https://doi.org/10.1039/D3EN00367A.
[31] A.O. Idris, E.O. Oseghe, T.A.M. Msagati, A.T. Kuvarega, U. Feleni, B. Mamba, Graphitic carbon nitride: a highly electroactive nanomaterial for environmental and clinical sensing, Sensors 20 (2020) 5743, https://doi.org/10.3390/s20205743.
[32] D. Prakashan, P. Kolhe, S. Gandhi, Design and fabrication of a competitive lateral flow assay using gold nanoparticle as capture probe for the rapid and on-site detection of penicillin antibiotic in food samples, Food Chem. 439 (2024) 138120, https://doi.org/10.1016/J.FOODCHEM.2023.138120.
[33] J.D. Henderson, L. Pearson, H. Nie, M.C. Biesinger, X-ray photoelectron spectroscopy analysis of indium and indium-containing compounds, Surf. Interface Anal. (2024) 81–97, https://doi.org/10.1002/sia.7356.
[34] A. Shrivastava, V. Gupta, Methods for the determination of limit of detection and limit of quantitation of the analytical methods, Chronicles Young Scientists 2 (2011) 21, https://doi.org/10.4103/2229-5186.79345.
[35] S. Krishnamurthy, A. Esterle, N.C. Sharma, S.V. Sahi, Yucca-derived synthesis of gold nanomaterial and their catalytic potential, Nanoscale Res. Lett. 9 (2014) 627, https://doi.org/10.1186/1556-276X-9-627.
[36] L. Florentino-Madiedo, E. Díaz-Faes, C. Barriocanal, Relationship between gCN structure and photocatalytic water splitting efficiency, Carbon N Y 187 (2022) 462–476, https://doi.org/10.1016/j.carbon.2021.11.030.
[37] J. Gubitosa, V. Rizzi, A. Laurenzana, F. Scavone, E. Frediani, G. Fibbi, F. Fanelli, T. Sibillano, C. Giannini, P. Fini, P. Cosma, The “end life” of the grape pomace waste become the new beginning: the development of a virtuous cycle for the green synthesis of gold nanoparticles and removal of emerging contaminants from water, Antioxidants 11 (2022) 994, https://doi.org/10.3390/antiox11050994.
[38] Y. Li, J. Zhang, Q. Wang, Y. Jin, D. Huang, Q. Cui, G. Zou, Nitrogen-rich carbon nitride hollow vessels: synthesis, characterization, and their properties, J. Phys. Chem. B 114 (2010) 9429–9434, https://doi.org/10.1021/jp103729c.
[39] S. Gurunathan, J. Han, J.H. Park, J.-H. Kim, A green chemistry approach for synthesizing biocompatible gold nanoparticles, Nanoscale Res. Lett. 9 (2014) 248, https://doi.org/10.1186/1556-276X-9-248.
[40] Y. Xu, Y. Gong, H. Ren, W. Liu, L. Niu, C. Li, X. Liu, In situ structural modification of graphitic carbon nitride by alkali halides and influence on photocatalytic activity, RSC Adv. 7 (2017) 32592–32600, https://doi.org/10.1039/C7RA05555B.
[41] D.A. Lomelí-Rosales, A. Zamudio-Ojeda, O.K. Reyes-Maldonado, M.E. López-Reyes, G.C. Basulto-Padilla, E.J. Lopez-Naranjo, V.M. Zuñiga-Mayo, G. Velázquez-Juárez, Green synthesis of gold and silver nanoparticles using leaf extract of Capsicum chinense plant, Molecules 27 (2022) 1692, https://doi.org/10.3390/molecules27051692.
[42] C. Karaman, B.B. Yola, O. Karaman, N. Atar, İ. Polat, M.L. Yola, Sensitive sandwich-type electrochemical SARS-CoV-2 nucleocapsid protein immunosensor, Microchim. Acta 188 (2021) 1–13, https://doi.org/10.1007/S00604-021-05092-6.
[43] G.C. Zaccariotto, M.K.L. Silva, G.S. Rocha, I. Cesarino, A Novel Method for the Detection of SARS-CoV-2 Based on Graphene-Impedimetric Immunosensor, Materials 14 (2021) 4230, https://doi.org/10.3390/MA14154230.
[44] E.B. Aydın, M. Aydın, M.K. Sezgintürk, Highly selective and sensitive sandwich immunosensor platform modified with MUA-capped GNPs for detection of spike receptor binding domain protein: a precious marker of COVID 19 infection, Sensors Actuators B Chem. 345 (2021) 130355, https://doi.org/10.1016/J.SNB.2021.130355.
[45] M. Mehmandoust, Z.P. Gumus, M. Soylak, N. Erk, Electrochemical immunosensor for rapid and highly sensitive detection of SARS-CoV-2 antigen in the nasal sample, Talanta 240 (2022) 123211, https://doi.org/10.1016/J.TALANTA.2022.123211.
[46] M. Adeel, K. Asif, V. Canzonieri, H.R. Barai, M.M. Rahman, S. Daniele, F. Rizzolio, Controlled, partially exfoliated, self-supported functionalized flexible graphitic carbon foil for ultrasensitive detection of SARS-CoV-2 spike protein, Sensors Actuators B Chem. 359 (2022) 131591, https://doi.org/10.1016/J.SNB.2022.131591.
[47] Z. Rahmati, M. Roushani, H. Hosseini, H. Choobin, An electrochemical immunosensor using SARS-CoV-2 spike protein-nickel hydroxide nanoparticles bio-conjugate modified SPCE for ultrasensitive detection of SARS-CoV-2 antibodies, Microchem. J. 170 (2021) 106718, https://doi.org/10.1016/J.MICROC.2021.106718.
[48] I. Ashur, J. Alter, M. Werbner, A. Ogungbile, M. Dessau, M. Gal-Tanamy, S. Vernick, Rapid electrochemical immunodetection of SARS-CoV-2 using a pseudo-typed vesicular stomatitis virus model, Talanta 239 (2022) 123147, https://doi.org/10.1016/J.TALANTA.2021.123147.
[49] Z. Rahmati, M. Roushani, H. Hosseini, H. Choobin, Electrochemical immunosensor with Cu2O nanocube coating for detection of SARS-CoV-2 spike protein, Microchim. Acta 188 (2021) 1–9, https://doi.org/10.1007/S00604-021-04762-9.
[50] W.A. El-Said, A.S. Al-Bogami, W. Alshitari, D.A. El-Hady, T.S. Saleh, M.A. El-Mokhtar, J.W. Choi, Electrochemical microbiosensor for detecting COVID-19 in a patient sample based on gold microcuboids pattern, Biochip J. 15 (2021) 287–295, https://doi.org/10.1007/S13206-021-00030-3.
[51] L.C. Brazaca, A.H. Imamura, N.O. Gomes, M.B. Almeida, D.T. Scheidt, P. A. Raymundo-Pereira, O.N. Oliveira, B.C. Janegitz, S.A.S. Machado, E. Carrilho, Electrochemical immunosensors using electrodeposited gold nanostructures for detecting the S proteins from SARS-CoV and SARS-CoV-2, Anal. Bioanal. Chem. 414 (2022) 5507–5517, https://doi.org/10.1007/S00216-022-03956-1.
[52] S. Ramanathan, S.C.B. Gopinath, Z. Hilmi Ismail, S. Subramaniam, Nanodiamond conjugated SARS-CoV-2 spike protein: electrochemical impedance immunosensing on a gold microelectrode, Microchim. Acta 189 (2022) 1–14, https://doi.org/10.1007/S00604-022-05320-7.
[53] S. Witt, A. Rogien, D. Werner, J. Siegenthaler, R. Lesiyon, N. Kurien, R. Rechenberg, N. Baule, A. Hardy, M. Becker, Boron doped diamond thin films for the electrochemical detection of SARS-CoV-2 S1 protein, Diam. Relat. Mater. 118 (2021) 108542, https://doi.org/10.1016/J.DIAMOND.2021.108542.
[54] P. Malla, H.P. Liao, C.H. Liu, W.C. Wu, P. Sreearunothai, Voltammetric biosensor for coronavirus spike protein using magnetic bead and screen-printed electrode for point-of-care diagnostics, Microchim. Acta 189 (2022) 1–12, https://doi.org/10.1007/S00604-022-05288-4.
[55] V. Ratautaite, R. Boguzaite, E. Brazys, D. Plausinaitis, S. Ramanavicius, U. Samukaite-Bubniene, M. Bechelany, A. Ramanavicius, Evaluation of the interaction between SARS-CoV-2 spike glycoproteins and the molecularly imprinted polypyrrole, Talanta 253 (2023) 123981, https://doi.org/10.1016/j.talanta.2022.123981.
[56] V. Ratautaite, R. Boguzaite, E. Brazys, A. Ramanaviciene, E. Ciplys, M. Juozapaitis, R. Slibinskas, M. Bechelany, A. Ramanavicius, Molecularly imprinted polypyrrole based sensor for the detection of SARS-CoV-2 spike glycoprotein, Electrochim. Acta 403 (2022) 139581, https://doi.org/10.1016/j.electacta.2021.139581.